



16 **Abstract**

17 Coseismic landslides have been responsible for destroyed buildings and structures, dislocated
18 roads and bridges, cut off of pipelines and lifelines, and tens of thousands of deaths. Newmark's
19 method is widely applied to assess the permanent displacement along a potential slide surface to
20 determine the coseismic responses of the slope. The M_w 6.1 (USGS) earthquake in Ludian,
21 Yunnan Province, China in 2014 has caused widespread landslides and provided the ideal data
22 sets to conduct a regional analysis of coseismic stability of slopes. The data sets include the
23 topography, shear strength, and ground shaking of the study area. All of these data sets are
24 digitized and rasterized at 30m grid spacing using ArcGIS and combined in a dynamic slope
25 model based on Newmark permanent-deformation analysis. The application of Barton model was
26 then applied in the permanent-deformation analysis. According to a method of inexact reasoning,
27 comparisons are made between the predicted displacements and a comprehensive inventory of
28 landslides triggered by the Ludian earthquake to map the spatial variability in certainty factors. A
29 coseismic landslide hazard map is then produced based on the spatial distribution of the values of
30 certainty factors. Such map can be applied to predict the hazard zone of the region and provide
31 guidelines for making decisions regarding infrastructure development and post-earthquake
32 reconstruction.

33

34 *Keywords:* Earthquakes; Landslides; Newmark's method; Barton model; Certainty factors;
35 Seismic hazards

36



37 **1. Introduction**

38 One of the major causes of landslides is recognized as the earthquake. Coseismic landslide
39 hazards have drawn increasing attention in recent years (i.e. Jibson et al., 1998; Khazai and Sitar,
40 2004; Qi et al., 2010, 2011, 2012; Xu et al., 2013; Chen et al., 2012; Yuan et al., 2014). In fact,
41 the damage caused by seismically triggered landslides is sometimes more severe than the
42 damage direct from the earthquake (Keefer, 1984). Estimating where is likely to trigger
43 landslides under a specific shaking condition plays an important role in regional seismic hazard
44 assessment (Jibson et al., 1998). Pseudostatic analysis formalized by Terzhagi (1950) and finite-
45 element modeling applied by Clough and Chopra (1966) were employed to assess the seismic
46 stability of slopes in early efforts. Newmark (1965) first introduced a relatively simple and
47 practical method, still commonly used, to estimate the coseismic permanent-displacements of
48 slopes. Studies showed that Newmark's method yields reasonable and practical results when
49 modeling the dynamic performance of natural slopes (Wilson and Keefer, 1983; Wieczorek et al.,
50 1985; Jibson et al., 1998, 2000; Pradel et al., 2005). Such applications generally start from an
51 analysis of the dynamic stability of slopes that is quantified as the critical acceleration. Barton
52 model has been widely used in rock mechanics and engineering field to predict the shear strength
53 of rock joints, which plays a crucial role in the calculation of critical acceleration. To better
54 estimate the dynamic stability of slopes, we introduce the Barton model into a Newmark analysis.
55 An improved modeling method is developed using data from the 2014 Ludian earthquake in
56 Yunnan Province, Southwestern China. Additionally, we present a method of inexact reasoning,
57 certainty factor model, to produce a probabilistic coseismic landslide hazard map.

58 This paper briefly introduces the site characteristics and the spatial distribution of triggered
59 landslides, describes the modeling method used for the analysis of seismic slope stability, then



60 presents the mapping procedure of the seismic slope-failure probability, and finally discusses the
61 results of the seismic hazard assessment and the application of the modeling procedure.

62

63 **2. Study area**

64 The epicenter of the 2014 M_w 6.1 Ludian earthquake is located in the southeastern margin of
65 the Tibetan plateau. A rectangular area lying immediately around the epicenter and containing
66 dense concentrations of induced landslides was chosen for study. Elevation in the study area
67 ranges from 785 m to 3,085 m above the sea. There are three rivers, the Niulanjiang River, the
68 Shaba River and the Longquan River passing through the area. The topography ranges from flat
69 in river valleys to nearly erect in the slopes on the side of the rivers. The Niulanjiang River,
70 flowing from southeast (SE) to the northwest (NW), where according to Chen et al. (2015),
71 incises down to a depth between 1,200 m and 3,300 m, resulting in about 80% of the slopes with
72 gradients greater than 40° distributed along the banks. Predominant geologic units of the study
73 area vary in the era from Proterozoic to Mesozoic, including basalt, sandstone, shale, limestone,
74 dolomite, and slate.

75 A landslide inventory containing 1,415 landslides (Fig. 1) was posed through comparison
76 between pre-earthquake and post-earthquake satellite images. The majority of landslides
77 triggered in this earthquake were shallow flow-like landslides (less than 3 m deep) developing in
78 particularly dense concentrations along steeply incised river valleys. The total area of these
79 interpreted landslides was 7.01 km^2 within a study area of 705 km^2 . A detailed study showed that
80 846 of the mapped landslides were greater than $1,000 \text{ m}^2$, occupying 6.74 km^2 and accounting
81 for 96.1% of the total landslide area, out of which 279 of the mapped landslides were greater
82 than $5,000 \text{ m}^2$, occupying 5.37 km^2 and accounting for 76.6% of the total landslide area.



83

84 **3. Methodology**

85 3.1 Modeling method

86 In the context of the analysis of the dynamic stability of a slope, Newmark (1965) proposed a
87 permanent-displacement analysis that bridges the gap between simplistic pseudostatic analysis
88 and sophisticated, but generally impractical finite-element modeling (Jibson, 1993). Newmark's
89 method simulates a landslide as a rigid-plastic friction block having a known critical acceleration
90 on an inclined plane (Fig. 2), and then calculates the cumulative permanent displacement of the
91 block as it is subjected to an acceleration-time history of an earthquake. Newmark (1965)
92 showed that the dynamic stability of a slope is related to the critical acceleration of a potential
93 landslide block, and it can be expressed as a simple function of the static factor of safety and the
94 landslide geometry as below:

$$a_c = (FS - 1)g \sin \alpha \quad (1)$$

95 where a_c is critical acceleration in terms of g , the acceleration due to earth's gravity, FS is static
96 factor of safety, and α is the angle from the horizontal that the center of the slide block moves
97 when displacement first occurs. For a planar slip surface parallel to the slope, this angle can
98 generally be approximated as the slope angle.

99 Natural slopes often develop a group of shallow unloading joints (Fig. 3) that parallel to the
100 surface due to valley incisions (Gu, 1979; Hoek and Bray, 1981). Studies showed that rock
101 slopes behave as collapsing and sliding failure of the shallow unloading joints under strong
102 earthquakes, and 90% of coseismic landslides are concentrated in the shallow of slopes (Harp
103 and Jibson, 1996; Khazai and Sitar, 2003; Dai et al., 2011; Tang et al., 2015). According to Qi et
104 al. (2012), there are two typical kinds of earthquake triggered landslides, i.e., (a) shallow flow-



105 like landslides with depth less than 3 m in general and (b) thrown landslides occurred at the crest
106 of the slope. For both types, the unstable rock blocks are often cut and activated along the rock
107 joints. Therefore, the static factor of safety in terms of the critical acceleration in these conditions
108 is related to the peak shear strength of the rock joints. For the purpose of regional stable analysis,
109 we use a limit-equilibrium model of an infinite slope (Fig. 2) referring to the simplification of
110 Jibson et al. (1998) on Newmark's method. On this occasion, the value of the static factor of
111 safety against sliding which is given by the ratio of resisting to driving force is determined by
112 conventional analysis with no consideration of horizontal or inclined accelerations, expressed as:

$$FS = \frac{\text{Resisting force}}{\text{Driving force}} = \frac{\tau L}{mg \sin \alpha} = \frac{\tau L}{\gamma L t \sin \alpha} = \frac{\tau}{\gamma t \sin \alpha} \quad (2)$$

113 where τ is peak shear strength of the rock joint, γ is unit weight of the rock mass, and t is the
114 thickness of the failure rock block.

115 For a Newmark analysis, it has been customary to describe the shear strength of rocks not rock
116 joints in terms of Coulomb's constants for friction and cohesion. However, both are not only
117 stress dependent variables, but also scale dependent (Barton and Choubey, 1977). According to
118 Barton (1973), a more satisfactory empirical relationship for predicting the peak shear strength of
119 a joint can be written as follows:

$$\tau = \sigma_n \tan [JRC \log_{10} \left(\frac{JCS}{\sigma_n} \right) + \phi_b] \quad (3)$$

120 where σ_n is effective normal stress, JRC is joint roughness coefficient, JCS is joint wall
121 compressive strength, ϕ_b is basic friction angle.

122 The effective normal stress (σ_n) generated by the gravity acting on the rock block is as follows:

$$\sigma_n = \frac{mg \cos \alpha}{L} = \frac{\gamma L t \cos \alpha}{L} = \gamma t \cos \alpha \quad (4)$$



123 Considering the impact of size effect on JRC and JCS , formulations were developed by Barton
 124 and Bandis (1982) and are shown as below:

$$JRC_n = JRC_0 \left(\frac{L_n}{L_0} \right)^{-0.02JRC_0} \quad (5)$$

$$JCS_n = JCS_0 \left(\frac{L_n}{L_0} \right)^{-0.03JRC_0} \quad (6)$$

125 where the nomenclature adopted incorporates the (l) and (n) for laboratory scale and in situ scale
 126 values respectively.

127 Hence the static factor of safety (FS) of a slope can be written as:

$$\begin{aligned} FS &= \frac{\tau}{\gamma t \sin \alpha} = \frac{\sigma_n \tan [JRC_n \log_{10} \left(\frac{JCS_n}{\sigma_n} \right) + \phi_b]}{\gamma t \sin \alpha} \\ &= \frac{\gamma t \cos \alpha \tan [JRC_n \log_{10} \left(\frac{JCS_n}{\gamma t \cos \alpha} \right) + \phi_b]}{\gamma t \sin \alpha} \\ &= \frac{\tan [JRC_n \log_{10} \left(\frac{JCS_n}{\gamma t \cos \alpha} \right) + \phi_b]}{\tan \alpha} \end{aligned} \quad (7)$$

128 After knowing the slope angle and the static factor of safety, the critical acceleration of a slope
 129 can be determined. Once the earthquake acceleration-time history has been selected, those
 130 portions of the record lying above the critical acceleration a_c (Fig. 4a) are integrated once to
 131 derive a velocity profile (Fig. 4b), which in turn is integrated a second time to obtain the
 132 cumulative displacement profile of the block (Fig. 4c). Users then judge the dynamic
 133 performance of a slope based on the magnitude of the Newmark displacement. The detailed
 134 procedure of conducting a Newmark analysis with Barton model is discussed in the following
 135 sections.

136 3.2 Static factor of safety



137 Considering that the mapped landslides greater than 1,000 m² occupy 96.1% of the total
138 landslide area, we selected a 30 m×30 m digital elevation model (DEM) ASTER Global Digital
139 Elevation Model (<https://doi.org/10.5067/ASTER/ASTGTM.002>, last accessed July 16, 2018)
140 that is capable of facilitating the subsequent hazard analysis. A basic slope algorithm was applied
141 to the DEM to produce a slope map (Fig. 5), where the slope is identified as the steepest
142 downhill descent from the cell to its neighbors (Burrough and McDonell, 1998). The slopes
143 range from greater than 60° in the banks of the Niulanjiang River, the Shaba River and the
144 Longquan River, to less than 20° in moderate and low mountains and hills in north and east.

145 Digital geologic map from China Geological Survey (GCS) was rasterized at 30 m grid
146 spacing for assigning material properties throughout the study area. According to the literature
147 researches, we found that JRC_0 and JCS_0 depend strongly on the lithology. Representative values
148 of γ , JRC_0 , JCS_0 and ϕ_b assigned to each rock type exposed in the area can normally be
149 estimated with the help of the test data listed in Table 1. The selected values were near the
150 middle of the ranges represented in the references. These JRC_0 and JCS_0 are considered in
151 laboratory scale, for the length of 100mm as L_0 . For each grid cell in regional analysis, L_n , the
152 length of engineering dimension, can generally be approximated as $\frac{30m}{\cos\alpha}$, where 30 m is the cell
153 size of the raster grid and α is the slope angle. The values of JRC_n and JCS_n , then, are calculated
154 by inserting values from JRC_0 , JCS_0 , L_0 , and L_n into Eq. (5) and Eq. (6). Fig. 6 shows the JRC_0
155 (Fig. 6a) and JCS_0 (Fig. 6b) values assigned to the rock types exposed in the study area, while
156 Fig. 7a and Fig. 7b show the JRC_n and JCS_n values respectively. The basic-friction-angle (ϕ_b)
157 map and unit weight (γ) map are shown as Fig. 8 and Fig. 9 respectively.

158 For simplicity, the thickness of the modeled block t was taken to be 3 m, which reflects the
159 typical slope failures of the Ludian earthquake. The static factor-of-safety map was produced by



160 combing these data layers (α , JRC_n , JCS_n , ϕ_b , and γ) in Eq. (7). In the initial iteration of the
161 calculation, static factors of safety ranged from 0.09 to 125.27. Grid cells in steep areas with
162 static factors of safety less than 1 indicate that the slopes are statically unstable, but do not
163 necessarily mean that the slopes are moving under the earthquake shaking. In this condition, to
164 avoid conservative results, we did not increase the strengths of rock types having statically
165 unstable cells, either, adjust strengths of other rock types to preserve the relative strength
166 differences between rock types. Instead we assigned a minimal static factor of safety as 1.01,
167 merely above limit equilibrium, to these slopes, to avoid a negative value of the critical
168 acceleration a_c . According to Keefer (1984), most landslides triggered by earthquakes occur
169 with a slope of 5° at least. Static factors of safety resulting from slopes less than 5° were very
170 high, and these slopes that were impossible to have failures under the Ludian earthquake did not
171 produce a statistically significant sample to the analysis. Therefore, slopes less than 5° were not
172 analyzed during the second iteration. After the adjustment, the static factors of safety ranged
173 from 1.0 to 8.5, as shown in Fig. 10.

174 3.3 Critical acceleration

175 According to Newmark (1965), a pseudostatic analysis in terms of the static factor of safety
176 and the slope angle was employed to calculate the critical acceleration of a potential landslide.
177 The critical-acceleration map (Fig. 11) was produced by combining the static factor of safety and
178 the slope angle in Eq. (1).

179 The critical acceleration that results in a static factor of safety of 1.0 and initiates a sliding of a
180 slope in a limit-equilibrium analysis is derived from the intrinsic slope properties (topography
181 and lithology), regardless which ground shaking is given. Therefore, the critical-acceleration
182 map indicates the susceptibility of the coseismic landslides (Jibson et al., 1998). The calculated



183 critical accelerations range from 6.35 g in areas that are more susceptible to coseismic landslides,
184 to almost zero in areas with lower susceptibility.

185 3.4 Shake map

186 There were 23 strong-motion stations within 100 km of the Ludian earthquake epicenter. Each
187 station record included three components of the peak ground acceleration (*PGA*), in south-north
188 direction, east-west direction and up-down direction respectively. We calculated the average
189 *PGA* of the two horizontal components of each strong-motion recording, and then plotted a
190 contour map (Fig. 12) using an Inverse Distance Weighted (IDW) interpolation algorithm. This
191 method assumes that the variable of the average *PGA* being mapped decreases in influence with
192 distance from its sampled location. Inverse Distance Weighted (IDW) interpolation determines
193 cell values using a linearly weighted combination of a set of sample stations (Watson and Philip,
194 1985). The weight is a function of inverse distance. In addition, considering that input stations
195 far away from the cell location where the prediction is being made may have poor or no spatial
196 correlation, we eliminated the input stations out of 100 km from the calculation.

197 3.5 Newmark displacement

198 In a real landslide hazard case, it is impossible to conduct a rigorous Newmark analysis when
199 accelerometer records are unavailable. It is also impractical and time consuming to produce a
200 displacement in each cell during the regional analysis. Therefore, empirical regressions
201 (Ambraseys and Menu, 1988; Jibson, 1993; Jibson et al., 1998; Saygili and Rathje, 2008; Rathje
202 and Saygili, 2009; Hsieh and Lee, 2011) were proposed to estimate Newmark displacement as a
203 function of the critical acceleration and peak ground acceleration or Arias intensity. Among
204 those empirical estimations, Rathje and Saygili (2009) developed a scalar model for



205 displacement in terms of the critical acceleration (a_c), peak ground acceleration (PGA) and
206 moment magnitude (M_w) based on analysis of over 2,000 strong motions.

$$\ln D = 4.89 - 4.85 \left(\frac{a_c}{PGA} \right) - 19.64 \left(\frac{a_c}{PGA} \right)^2 + 42.49 \left(\frac{a_c}{PGA} \right)^3 - 29.06 \left(\frac{a_c}{PGA} \right)^4 + 0.72 \ln(PGA) + 0.89(M_w - 6) \quad (8)$$

207 where D is predicted displacement in units of cm , a_c and PGA are in units of g .

208 This model is a preferred displacement model at a specific site where acceleration-time
209 recordings are not available. The incorporating multiple ground motion parameters in the
210 analysis typically results in less variability in the prediction of displacement (Rathje and Saygili,
211 2009).

212 The Newmark displacement (Fig. 13) in each cell was calculated by combing corresponding
213 values of the critical acceleration, peak ground acceleration and moment magnitude in Eq (8).
214 Predicted displacements range from 0 cm to 123 cm.

215 3.6 Certainty factor and coseismic landslide hazard map

216 According to Jibson et al. (1998), predicted displacements provide an index of seismic
217 performance of slopes, but do not correspond directly to measurable slope movements in the
218 field. Therefore, larger predicted displacements do not necessarily relate to greater incidence of
219 slope failures. To produce a coseismic landslide hazard map, we chose a model of inexact
220 reasoning, the certainty factor model (CFM), which was created by Shortliffe and Buchanan
221 (1975) and improved by Hecherman (1986), to explore the relationship between the landslide
222 occurrences and the predicted displacements. The CFM was created as a numerical method,
223 which was initially used by MYCIN, a backward chaining expert system in medicine (Shortliffe
224 and Buchanan, 1975), for managing uncertainty in a rule-based system. In this model, the
225 certainty factor CF represents the net belief in a hypothesis H based on the evidence E



226 (Hecherman, 1986). Certainty factors range between -1 and 1. A *CF* with a value of -1 means
227 total disbelief, whereas a *CF* with a value of 1 means total belief. Values greater than 0 favor the
228 hypothesis while values less than 0 favor the negation of the hypothesis. According to
229 Hecherman (1986), there is a probabilistic interpretation for *CF* shown as below:

$$CF = \begin{cases} \frac{p(H|E) - p(H)}{p(H|E)[1 - p(H)]}, & p(H|E) > p(H) \\ \frac{p(H|E) - p(H)}{p(H)[1 - p(H|E)]}, & p(H|E) < p(H) \end{cases} \quad (9)$$

230 where *CF* is the certainty factor, $p(H|E)$ denotes the conditional probability for the case of a
231 posterior hypothesis that relies on evidence, the posterior probability, and $p(H)$ is the prior
232 probability before any evidence is known. In the displacement analysis, $p(H|E)$ was defined as
233 the proportion of the landslide area within a specific displacement area while $p(H)$ was defined
234 as the proportion of the landslide area within the entire study area excluding the slopes less than
235 5°. In this way, values of *CF* represent the probability of coseismic landslides. Positive values
236 correspond to an increase in probability in a slope failure while negative quantities correspond to
237 a decrease in probability. Greater positive values indicate higher probability of coseismic
238 landslides.

239 Given this definition, we could produce a coseismic landslide hazard map in terms of certainty
240 factors. First, displacement cells in every 1 cm were grouped into bins, such that all cells having
241 displacements between 0 cm and 1cm were grouped into the first bin; those having
242 displacements between 1 cm and 2 cm were grouped into the second bin, and so on. The
243 displacements were grouped into 123 bins, from 0 cm to 123 cm except for 122 cm (no predicted
244 displacement in 122 cm). Later, we calculated the proportion of landslide cells in each bin. This
245 proportion was considered the posterior probability of each bin as defined. The prior probability



246 calculated by dividing the entire landslide area by the entire study area is same in each bin.
247 Finally, values of CF were computed in each bin by using Eq. (9) to combine corresponding
248 values of the posterior probability and prior probability. Certainty factors range from -1.00 to
249 0.83. Values of CF indicate probabilities of landslide occurrence of each bin in the study area
250 and provide the basis for producing a coseismic landslide hazard map.

251 As shown in the hazard map for the Ludian earthquake (Fig. 14), most of the actual triggered
252 landslides lie in the higher probability areas with CF values greater than 0.60. The interpreted
253 landslides are covered on the map to demonstrate the good fit for predicted probabilities of
254 coseismic landslides.

255

256 **4. Results and Discussion**

257 The predicted displacements represent the cumulative sliding displacements for a given
258 acceleration-time history. Based on the statistically significant sizes of the area of each
259 displacement shown in Fig. 15, we conclude that the study area would probably suffer from
260 different types of coseismic landslides. The vast majority of area are from displacements that less
261 than the middle of the ranges. Displacements around 60 cm have the largest area, and
262 displacements less than 2 cm have the second largest area, while displacements greater than 90
263 cm occupy a very small area. Jibson et al. (1998) supposed that shallow falls and slides in brittle,
264 weakly cemented materials would fail at a relatively small displacement, while slumps and block
265 slides in more compliant materials would likely fail at a larger displacement. That is to say, the
266 study area is more susceptible to rock falls and shallow, disrupted slides that fail at a relatively
267 small displacement, while the study area is with a lower probability subjected to coherent, deep-
268 seated slides that would fail at a larger displacement. Indeed, the majority of landslides triggered



269 by the Ludian earthquake were shallow, disrupted slides and rock falls (Zhou et al., 2016).
270 Although few catastrophic rock avalanches, such as the Hongshiyuan landslide (Chang et al.,
271 2017), occurred in the field, they did not produce statistically significant samples that could
272 meaningfully contribute to the model, which was consistent with the statistic results as discussed
273 previously. Therefore, the model should relate well to typical kinds of earthquake-induced
274 landslides in the study area, meanwhile demonstrate its potential utility to predict the probability
275 of other types of landslides.

276 For each value of CF , the proportion of landslide area was plotted as a dot in Fig. 16. The data
277 was fitted by a second order exponential growth function. The fitting appears to be very good:
278 the proportion of landslide area within each CF -value area increases exponentially with the
279 increase of the value of CF . When the value of CF is reaching 1.0 (total belief) in Fig. 16, the
280 proportion of landslide area is monotonically getting close to 1.0, which means the probability of
281 a slope failure is growing and a landslide would probably occur. Such a procedure is consistent
282 with the interpretation of the certainty factor theory. Therefore, the CFM demonstrates the
283 capability of its representation and predicting approach for a probabilistic hazard analysis of
284 coseismic landslides.

285 When fitting the results of shear tests using Coulomb's linear relation, the shear strengths vary
286 widely from high normal stress in laboratory to low normal stress in the field (Barton, 1973). We
287 introduced Barton model into the Newmark analysis to reduce the variability of shear strengths
288 in terms of Coulomb's constants. And we considered the impact of scale effects by using Eq. (5)
289 and Eq. (6), which helps to prevent Newmark's method from underestimating the shear strength
290 of geologic units in a regional analysis. In addition, for Barton model, the joint roughness
291 coefficient (JRC) could be estimated from tilt tests or from matching of Barton joint standard



292 roughness profiles that were regarded by the International Society for Rock Mechanics (ISRM,
293 1978), while the joint wall compressive strength (*JCS*) could be estimated by Schmidt hammer
294 index tests. These tests are helpful to make a quick estimate of the shear strength in situ, which
295 could facilitate using Newmark's method in an emergency hazard and risk assessment after an
296 earthquake.

297 Shear strengths assigned to the geologic units were from results of hundreds of shear tests
298 from the references. Although the assigned shear strengths would have uncertainty in some way,
299 the good fit of the spatial distribution of coseismic landslides shown by the probabilistic hazard
300 map (Fig. 15) demonstrates the practicability of Barton model in the analysis.

301

302 **5. Conclusion**

303 Newmark's method is a useful, physically based model to estimate the seismic stability of
304 natural slopes. Mapping procedure of data from the Ludian earthquake shows the feasibility of
305 Barton model in a Newmark analysis. Such method decreases the uncertainty of shear strengths
306 in a Newmark model and provides practical applications in regional seismic hazard assessment.
307 We also consider the size effect of shear strength parameters, such as the joint roughness
308 coefficient (*JRC*) and the joint wall compressive strength (*JCS*) in a regional analysis. Moreover,
309 the linkage of Newmark displacements to certainty factor model improves the utility of
310 Newmark's method to predict the probabilistic hazard of coseismic landslides.

311

312 **Acknowledgements**

313 This work is supported by Natural Science Foundation of China under Grants of Nos.
314 41825018 and 41672307, Science and Technology Service Network Initiative under Grant No.



315 KFJ-EW-ST5-094, and the sponsorship from the China Scholarship Council (No.
316 201704910537).

317



318 **References**

- 319 Alejano, L. R., González, J. and Muralha, J.: Comparison of different techniques of tilt testing
320 and basic friction angle variability assessment. *Rock mechanics and rock engineering* 45(6),
321 1023-1035, 2012.
- 322 Alejano, L. R., Perucho, Á., Olalla, C. and Jiménez, R.: *Rock engineering and rock mechanics:*
323 *structures in and on rock masses.* CRC Press, Boca Raton, Florida, 615-1148, 2014.
- 324 Ambraseys, N. N. and Menu, J. M.: Earthquake-induced ground displacements. *Earthquake*
325 *engineering and structural dynamics* 16(7), 985-1006, 1988.
- 326 Bandis, S. C., Lumsden, A. C. and Barton, N. R.: Fundamentals of rock joint deformation.
327 *International Journal of Rock Mechanics and Mining Sciences & Geomechanics Abstracts*
328 20(6), 249-268, 1983.
- 329 Barton, N.: Review of a new shear-strength criterion for rock joints. *Engineering geology* 7(4),
330 287-332, 1973.
- 331 Barton, N. and Bandis, S.: Effects of block size on the shear behavior of jointed rock. Keynote
332 Lecture in the 23rd US Symposium on Rock Mechanics (USRMS). American Rock
333 Mechanics Association, Berkeley, California, 739-760, 1982.
- 334 Barton, N. and Choubey, V.: The shear strength of rock joints in theory and practice. *Rock*
335 *mechanics* 10(1-2), 1-54, 1977.
- 336 Bilgin, H. A. and Pasamehmetoglu, A. G.: Shear behaviour of shale joints under heat in direct
337 shear. In Barton N. and Stephansson O. (Eds.), *Rock joints.* CRC Press, Rotterdam, 179-183,
338 1990.
- 339 Burrough P. A. and McDonnell R. A.: *Principles of geographical information systems* (2nd
340 Edition). Oxford University Press, New York, 190, 1998.



- 341 Chang, Z. F., Chang, H., Yang, S. Y., Chen, G. and Li, J. L.: Characteristics and formation
342 mechanism of large rock avalanches triggered by the Ludian Ms6.5 earthquake at Hongshiyuan
343 and Ganjiazhai. *Seismology and Geology* 39(5), 1030-1047, 2017 (in Chinese with English
344 abstract).
- 345 Chen, X. L., Ran, H. L. and Yang, W. T.: Evaluation of factors controlling large earthquake-
346 induced landslides by the Wenchuan earthquake. *Natural Hazards and Earth System Sciences*,
347 12(12), 3645-3657, 2012.
- 348 Chen, X. L., Zhou, Q. and Liu, C. G.: Distribution pattern of coseismic landslides triggered by
349 the 2014 Ludian, Yunnan, China Mw6.1 earthquake: special controlling conditions of local
350 topography. *Landslides* 12(6), 1159-1168, 2015.
- 351 Clough, R. W. and Chopra, A. K.: Earthquake stress analysis in earth dams. *ASCE Journal of the*
352 *Engineering Mechanics Division* 92, 197-211, 1966.
- 353 Coulson, J.H.: Shear strength of flat surfaces in rock. In Cording, E. J. (Ed.), *Stability of Rock*
354 *Slopes*. 13th Symposium on Rock Mechanics, Urbana, Illinois, 77-105, 1972.
- 355 Dai, F. C., Xu, C., Yao, X., Xu, L., Tu, X. B. and Gong, Q. M.: Spatial distribution of landslides
356 triggered by the 2008 Ms 8.0 Wenchuan earthquake, China. *Journal of Asian Earth Sciences*
357 40(4), 883-895, 2011.
- 358 Giusepone, F. and da Silva, L. A. A.: Hoek & Brown and Barton & Bandis Criteria Applied to a
359 Planar Sliding at a Dolomite Mine in Gandarela Synclinal. In *ISRM Conference on Rock*
360 *Mechanics for Natural Resources and Infrastructure-SBMR 2014*. International Society for
361 *Rock Mechanics*, 2014.
- 362 Gu, D. Z.: *Engineering geomechanics of rock mass*. Science Press, Beijing, China, 1979 (in
363 Chinese).



- 364 Harp, E. L. and Jibson, R. W.: Landslides triggered by the 1994 Northridge, California,
365 earthquake. *Bulletin of the Seismological Society of America* 86(1B), S319-S332, 1996.
- 366 Heckerman, D.: Probabilistic interpretations for MYCIN's certainty factors. In Kanal, L. N. and
367 Lemmer, J. F. (Eds), *Machine Intelligence and Pattern Recognition 4*, North-Holland, 167-
368 196, 1986.
- 369 Hsieh, S. Y. and Lee, C. T.: Empirical estimation of the Newmark displacement from the Arias
370 intensity and critical acceleration. *Engineering Geology* 122(1-2), 34-42, 2011.
- 371 Hoek, E. and Bray, J. D.: *Rock slope engineering*. CRC Press, 1981.
- 372 ISRM (International Society for Rock Mechanics): Suggested Methods for the Quantitative
373 Description of Discontinuities in Rock Masses. *International Journal of Rock Mechanics and*
374 *Mining Sciences & Geomechanics Abstracts* 15, 319-368, 1978.
- 375 Jibson, R. W.: Predicting earthquake-induced landslide displacements using Newmark's sliding
376 block analysis. *Transportation research record* 1411, 9-17, 1993.
- 377 Jibson, R. W., Harp, E. L. and Michael, J. A.: A method for producing digital probabilistic
378 seismic landslide hazard maps: an example from the Los Angeles, California, area. US
379 Geological Survey. Open-File Rep. 98-113. 17 pp., 1998.
- 380 Jibson, R. W., Harp, E. L. and Michael, J. A.: A method for producing digital probabilistic
381 seismic landslide hazard maps. *Engineering Geology* 58(3-4), 271-289, 2000.
- 382 Keefer, D. K.: Landslides caused by earthquakes. *Geological Society of America Bulletin* 95(4),
383 406-421, 1984.
- 384 Khazai, B. and Sitar, N.: Evaluation of factors controlling earthquake-induced landslides caused
385 by Chi-Chi earthquake and comparison with the Northridge and Loma Prieta events.
386 *Engineering geology* 71(1-2), 79-95, 2004.



- 387 NASA/METI/AIST/Japan Spacesystems and U.S./Japan ASTER Science Team: ASTER Global
388 Digital Elevation Model version 2. NASA EOSDIS Land Processes DAAC, [https://doi:](https://doi.org/10.5067/ASTER/ASTGTM.002)
389 10.5067/ASTER/ASTGTM.002 (last accessed July 16, 2018), 2009.
- 390 Newmark, N. M.: Effects of earthquakes on dams and embankments. *Geotechnique* 15(2), 139-
391 160, 1965.
- 392 Pradel, D., Smith, P. M., Stewart, J. P. and Raad, G.: Case history of landslide movement during
393 the Northridge earthquake. *Journal of Geotechnical and Geoenvironmental Engineering*
394 131(11), 1360-1369, 2005.
- 395 Priest, S. D.: *Discontinuity analysis for rock engineering*. Springer Science & Business Media,
396 B.V., Dordrecht, 320, 2012.
- 397 Qi, S. W., Xu, Q., Lan, H. X., Zhang, B. and Liu, J. Y.: Spatial distribution analysis of landslides
398 triggered by 2008.5.12 Wenchuan Earthquake, China, *Engineering Geology* 116 (1-2),
399 95~108, 2010.
- 400 Qi, S. W., Xu, Q., Zhang, B., Zhou, Y. D., Lan, H. X. and Li, L. H.: Source characteristics of
401 long runout rock avalanches triggered by the 2008 Wenchuan earthquake, China, *Journal of*
402 *Asian Earth Sciences* 40 (4), 896~906, 2011.
- 403 Qi, S. W., Yan, C. G. and Liu, C. L.: Two typical types of earthquake triggered landslides and
404 their mechanisms. In *Landslides and Engineered Slopes: Protecting Society through Improved*
405 *Understanding*, ISBN 978-0-415-63303-1, 2012.
- 406 Rathje, E. M. and Saygili, G.: Probabilistic assessment of earthquake-induced sliding
407 displacements of natural slopes. *Bulletin of the New Zealand Society for Earthquake*
408 *Engineering* 42(1), 18-27, 2009.



- 409 Saygili, G. and Rathje, E. M.: Empirical predictive models for earthquake-induced sliding
410 displacements of slopes. *Journal of Geotechnical and Geoenvironmental Engineering* 134(6),
411 790-803, 2008.
- 412 Shortliffe, E. H. and Buchanan, B. G.: A model of inexact reasoning in medicine. *Mathematical*
413 *Biosciences* 23, 351-379, 1975.
- 414 Singh, T. N., Kainthola, A. and Venkatesh, A.: Correlation between point load index and
415 uniaxial compressive strength for different rock types. *Rock Mechanics and Rock*
416 *Engineering* 45(2), 259-264, 2012.
- 417 Tang, C., Ma, G., Chang, M., Li, W., Zhang, D., Jia, T. and Zhou, Z.: Landslides triggered by the
418 20 April 2013 Lushan earthquake, Sichuan Province, China. *Engineering Geology* 187, 45-55,
419 2015.
- 420 Terzhagi, K.: Mechanism of landslides. In Paige, S. (Ed.), *Application of Geology to*
421 *Engineering Practice (Berkey Volume)*. Geological Society of America, New York, NY, 83-
422 123, 1950.
- 423 Watson, D. F. and Philip, G. M.: A Refinement of Inverse Distance Weighted Interpolation.
424 *Geoprocessing* 2, 315–327, 1985.
- 425 Wieczorek, G. F., Wilson, R. C. and Harp, E. L.: Map showing slope stability during earthquakes
426 in San Mateo County, California. U.S. Geological Survey Miscellaneous Investigations Map
427 I-1257-E, scale 1:62,500, 1985.
- 428 Wilson, R. C. and Keefer, D. K.: Dynamic analysis of a slope failure from the 6 August 1979
429 Coyote Lake, California, earthquake. *Bulletin of the Seismological Society of America* 73(3),
430 863-877, 1983.



- 431 Xu, C., Xu, X., Zhou, B., and Yu, G.: Revisions of the M 8.0 Wenchuan earthquake seismic
432 intensity map based on co-seismic landslide abundance. *Natural Hazards*, 69(3), 1459-1476,
433 2013.
- 434 Yong, R., Ye, J., Liang, Q. F., Huang, M. and Du, S. G.: Estimation of the joint roughness
435 coefficient (JRC) of rock joints by vector similarity measures. *Bulletin of Engineering
436 Geology and the Environment* 77, 735-749, 2018.
- 437 Yuan, R. M., Tang, C. L., Hu, J. C., and Xu, X. W.: Mechanism of the Donghekou landslide
438 triggered by the 2008 Wenchuan earthquake revealed by discrete element modeling. *Natural
439 Hazards and Earth System Sciences*, 14(5), 1195-1205, 2014.
- 440 Zhou, S. H., Chen, G. Q. and Fang, L. G.: Distribution pattern of landslides triggered by the
441 2014 Ludian earthquake of China: Implications for regional threshold topography and the
442 seismogenic fault identification. *ISPRS International Journal of Geo-Information* 5(4), 46,
443 2016.
- 444



445 **Figure Captions**

446 **Fig. 1.** Map of the study area showing interpreted landslides.

447 **Fig. 2.** Conceptual sliding-block model of a Newmark analysis.

448 **Fig. 3.** A schematic diagram showing shadow unloading joints in the slope.

449 **Fig. 4.** Demonstration of the Newmark-analysis algorithm (adapted from Wilson and Keefer,
450 1983)

451 **Fig. 5.** Slope map derived from the DEM of the study area.

452 **Fig. 6.** (a) JRC_0 and (b) JCS_0 assigned to rock types in the study area.

453 **Fig. 7.** (a) JRC_n component and (b) JCS_n component of shear strength assigned to rock types in
454 the study area.

455 **Fig. 8.** Basic-friction-angle (ϕ_b) component of shear strength assigned to rock types in the study
456 area.

457 **Fig. 9.** Unit weight (γ) assigned to rock types in the study area.

458 **Fig. 10.** Static factor-of-safety map of the study area.

459 **Fig. 11.** Map showing critical accelerations in the study area.

460 **Fig. 12.** Contour map of peak ground acceleration (PGA) produced by the Ludian earthquake in
461 the study area. PGA values shown are in g .

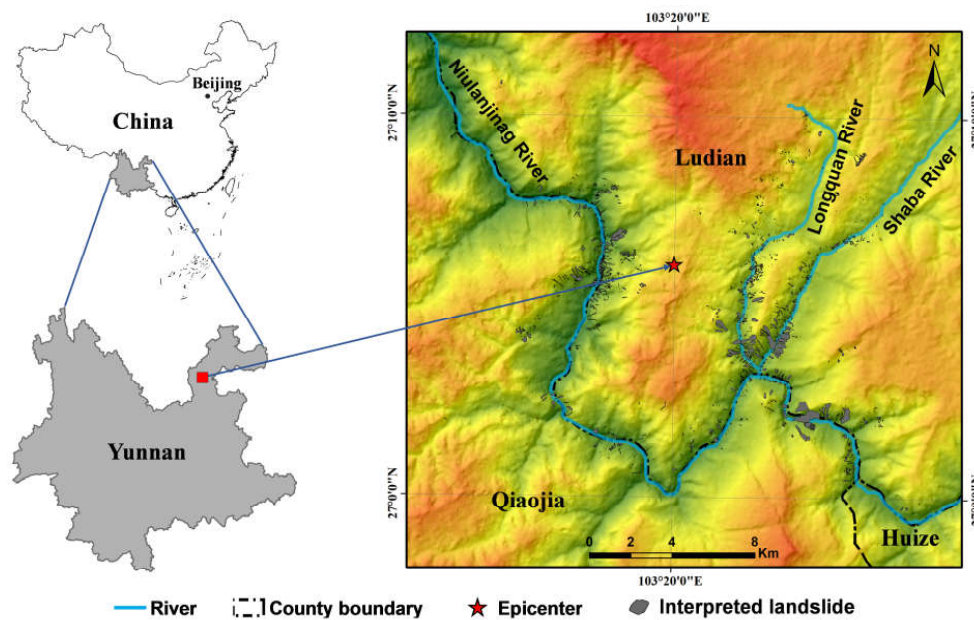
462 **Fig. 13.** Map showing predicted displacements in the study area.

463 **Fig. 14.** Map showing probability of coseismic landslides in the Ludian earthquake. Probability
464 is portrayed in terms of values of CF .

465 **Fig. 15.** Statistics data display the area of each predicted displacement.



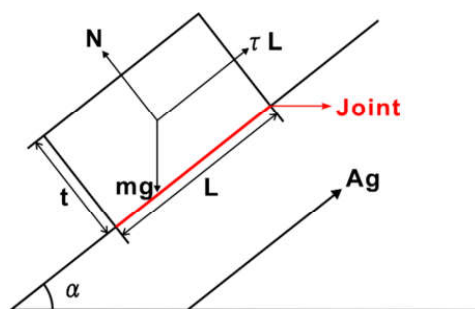
466 **Fig. 16.** Proportion of the area of landslides lying in each CF -value area. A dot shows the
467 proportion of landslide area within an area of CF value; the red line is the fitting curve of the
468 data using second order exponential growth function.



469

470 **Fig. 1.** Map of the study area showing interpreted landslides.

471



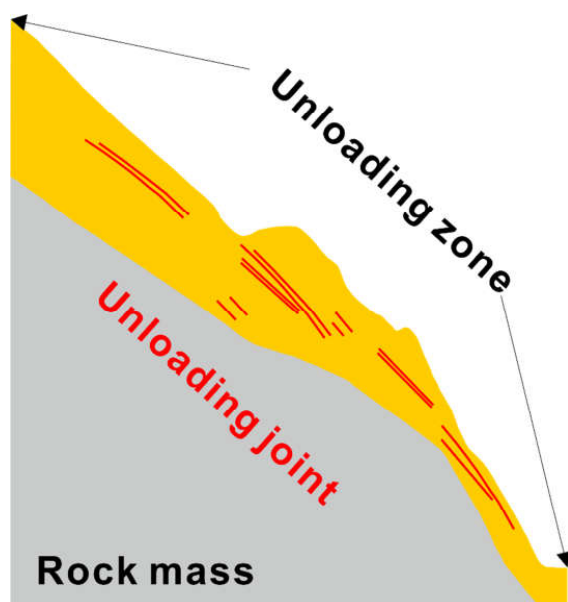
472

473 **Fig. 2.** Conceptual sliding-block model of a Newmark analysis. The potential landslide is

474 modeled as a rigid-plastic block resting on an inclined plane at an angle (α) from the horizontal.

475 The base of the block is subjected to an earthquake ground acceleration that is denoted by A_g .

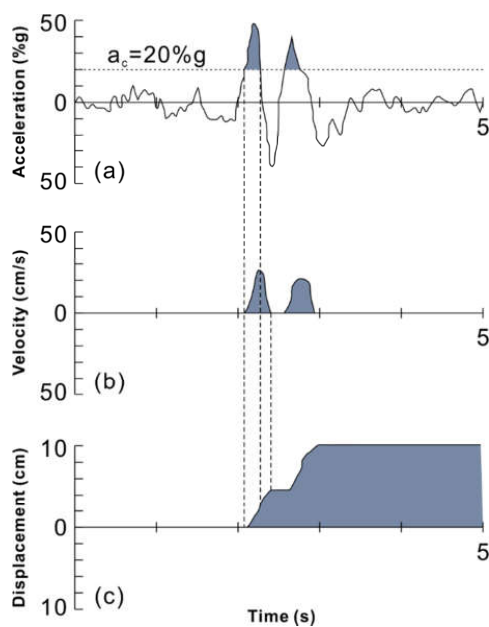
476



477

478 **Fig. 3.** A schematic diagram showing shadow unloading joints in the slope.

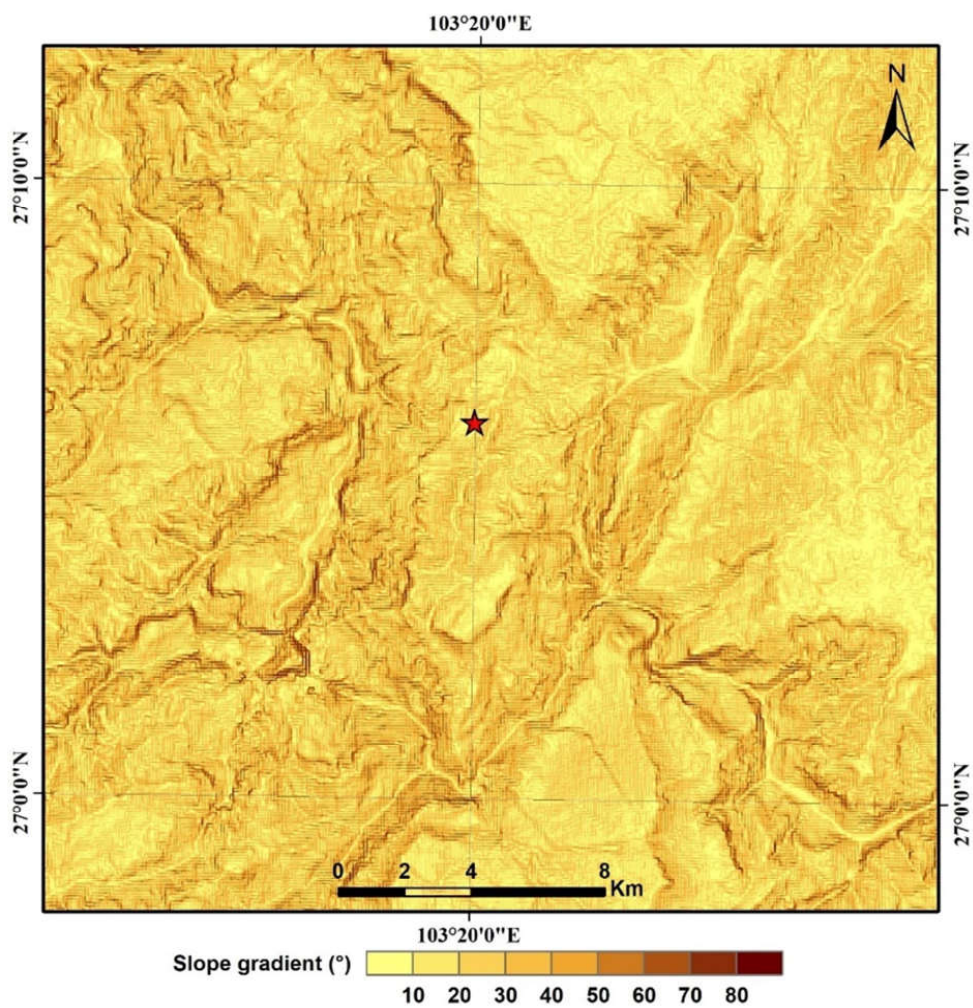
479



480

481 **Fig. 4.** Demonstration of the Newmark-analysis algorithm (adapted from Wilson and Keefer,
482 1983): (a) Acceleration-time history with critical acceleration (horizontal dotted line) of 20%g
483 superimposed. (b) Velocity of block versus time. (c) Displacement of block versus time.

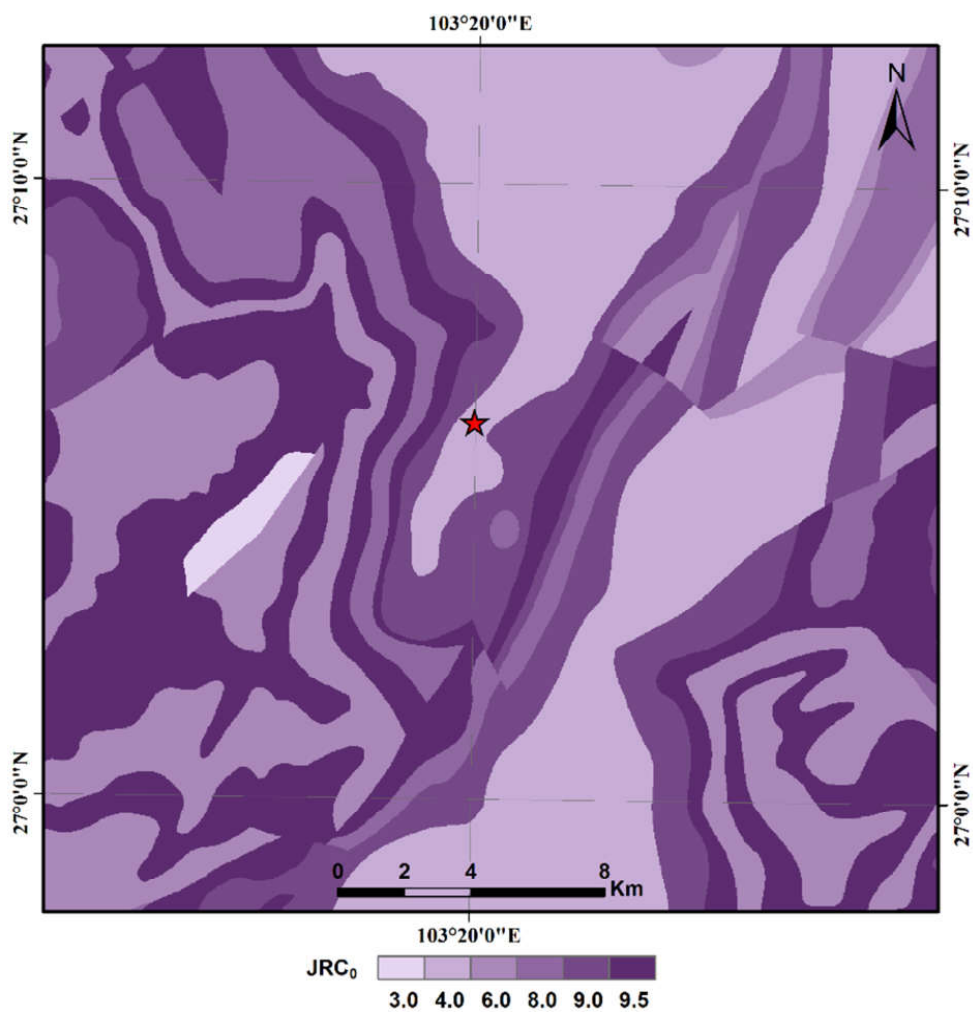
484



485

486 **Fig. 5.** Slope map derived from the DEM of the study area.

487



(a)

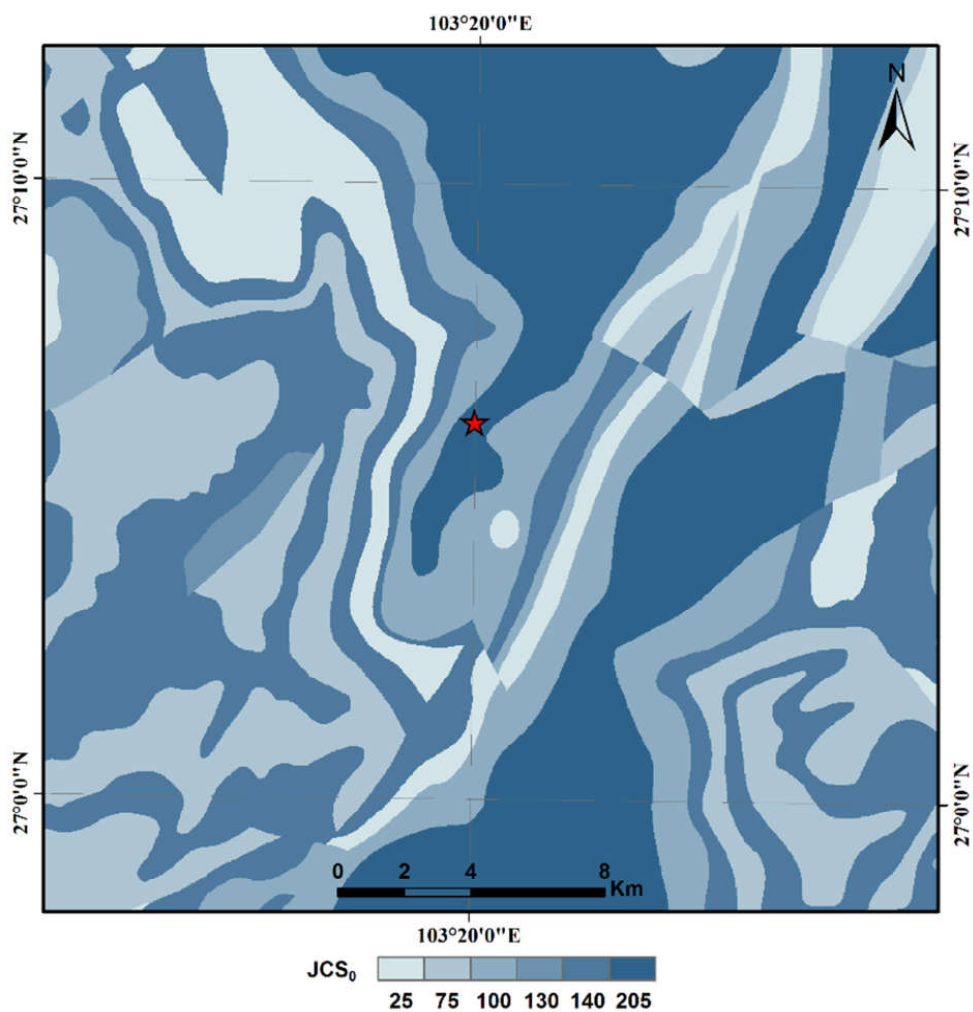
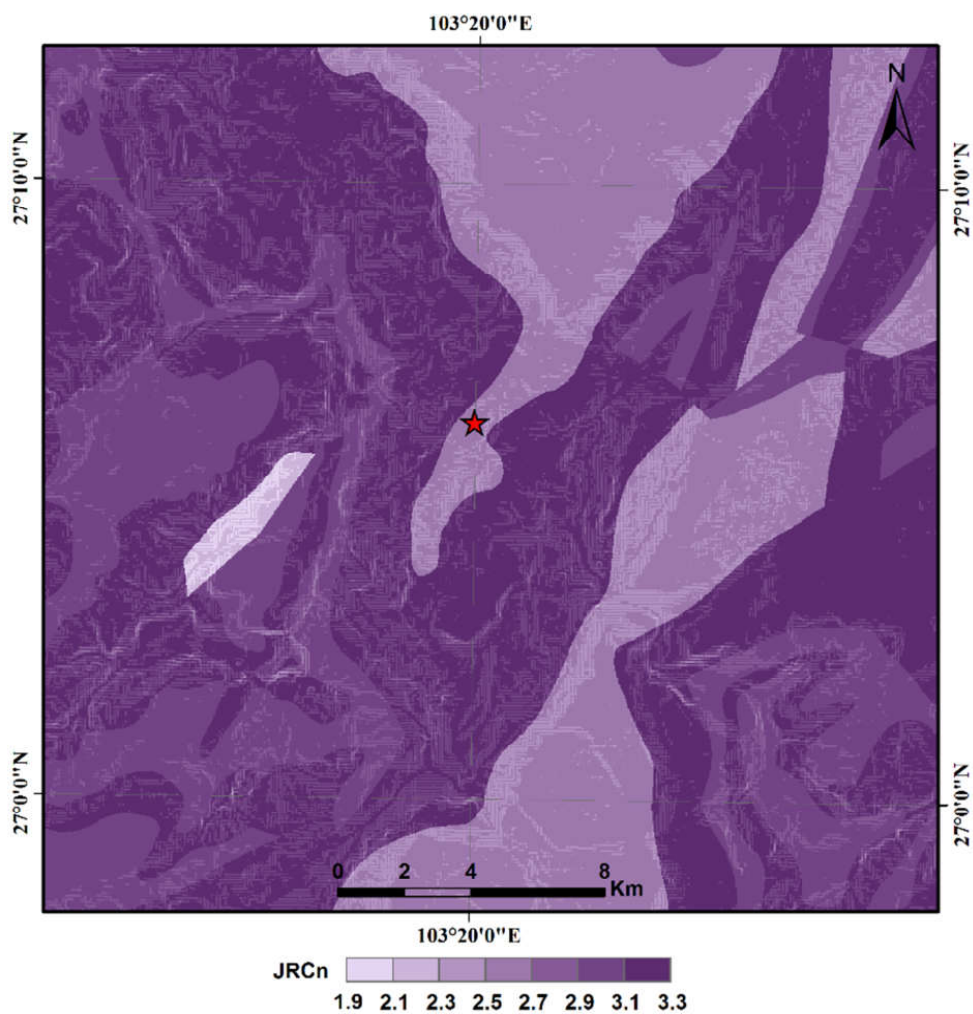
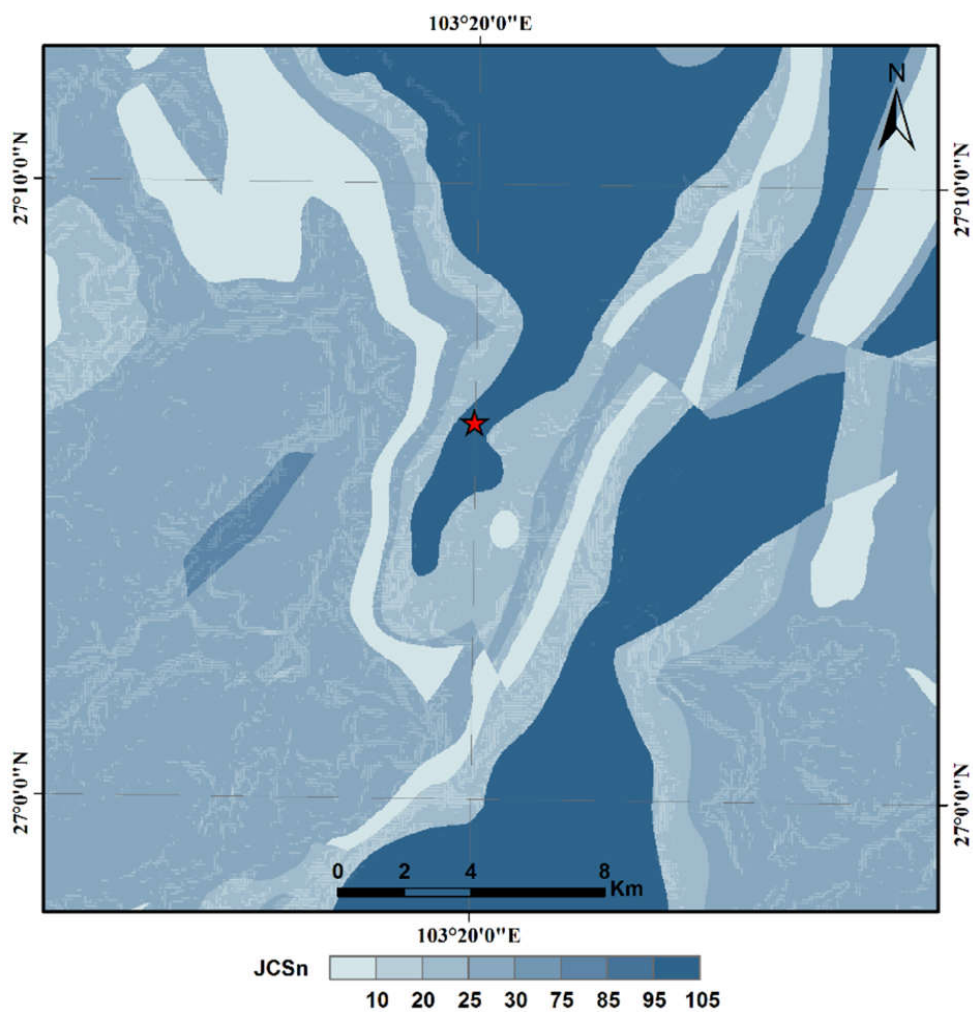


Fig. 6. (a) JRC_0 and (b) JCS_0 assigned to rock types in the study area.



(a)



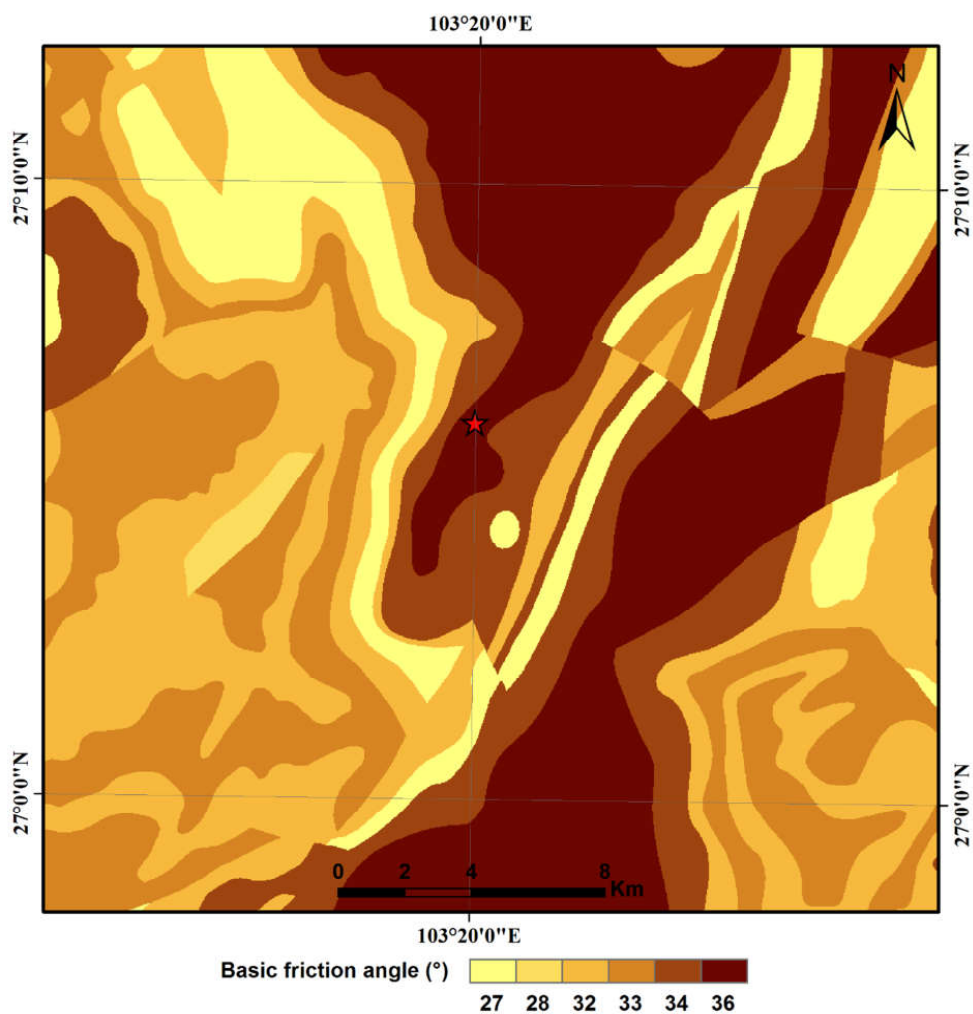
496

497

498 **Fig. 7.** (a) JRC_n component and (b) JCS_n component of shear strength assigned to rock types in

499 the study area.

500

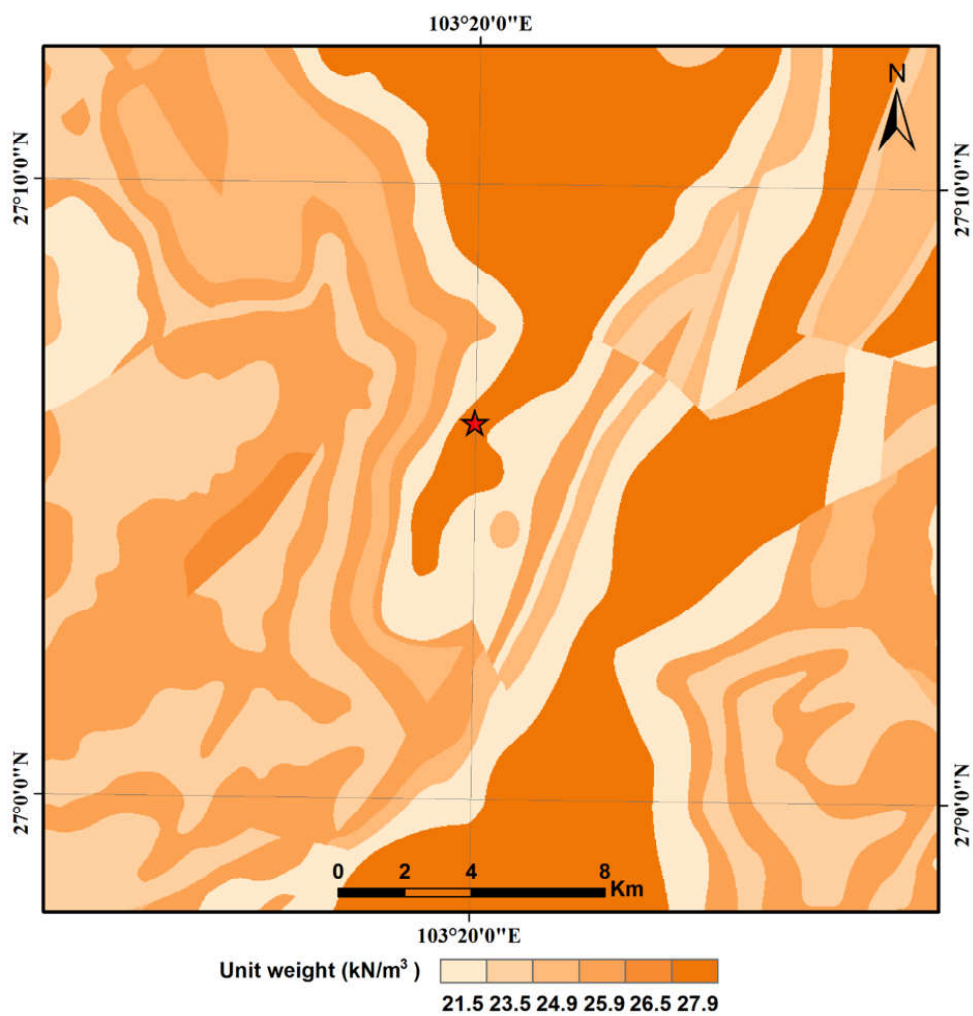


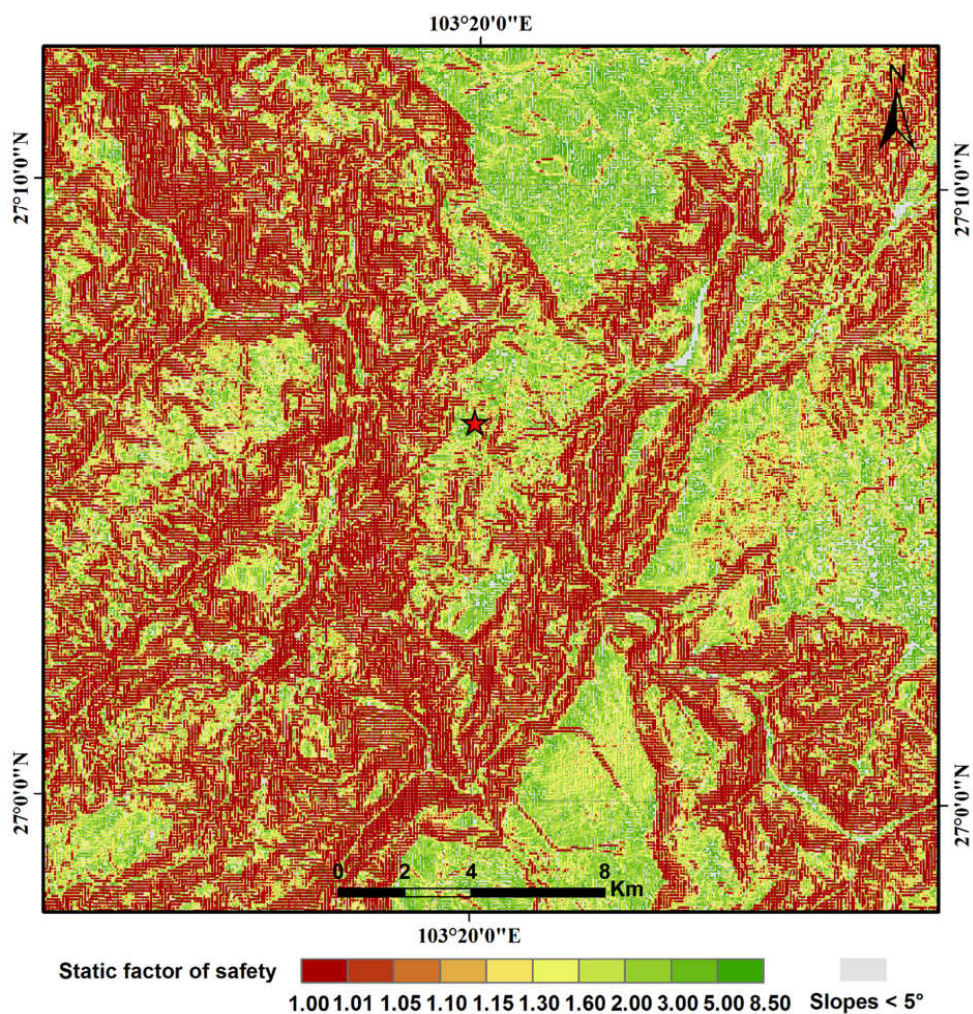
501

502 **Fig. 8.** Basic-friction-angle (ϕ_b) component of shear strength assigned to rock types in the study

503 area.

504

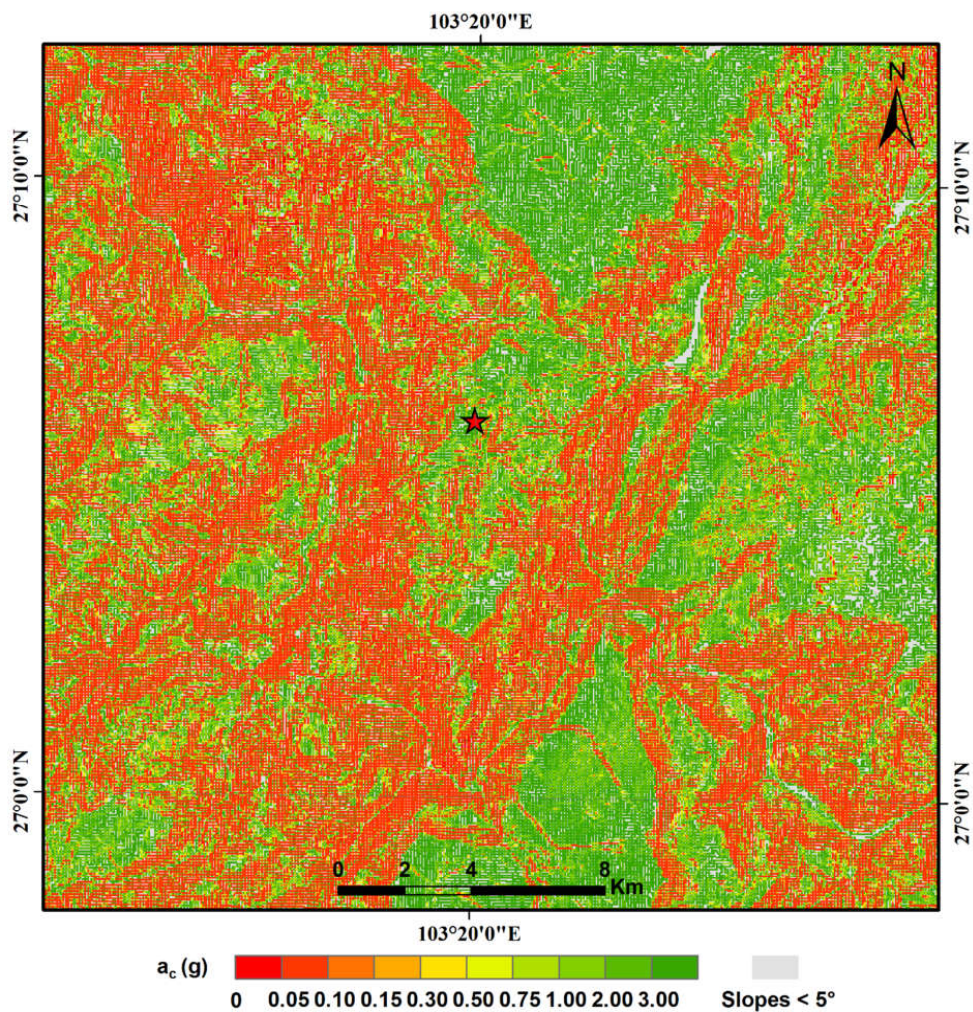




508

509 **Fig. 10.** Static factor-of-safety map of the study area.

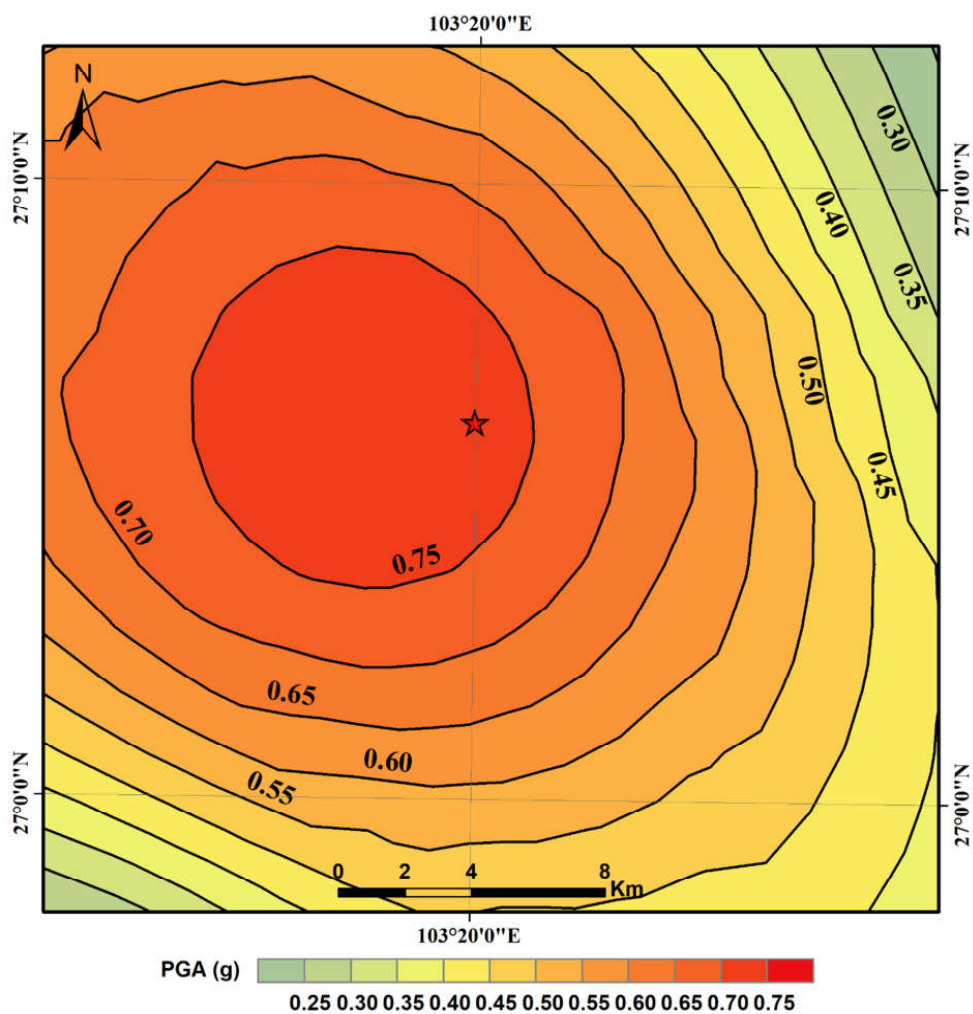
510

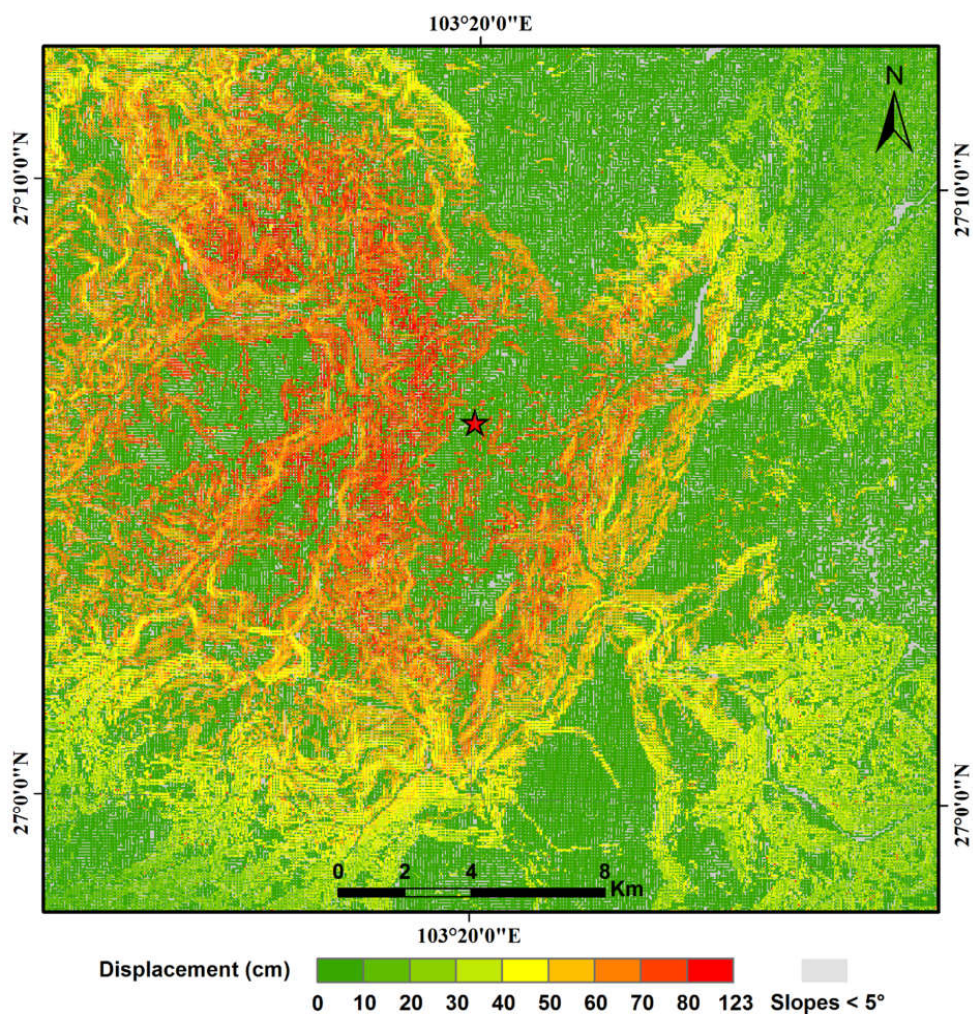


511

512 **Fig. 11.** Map showing critical accelerations in the study area.

513

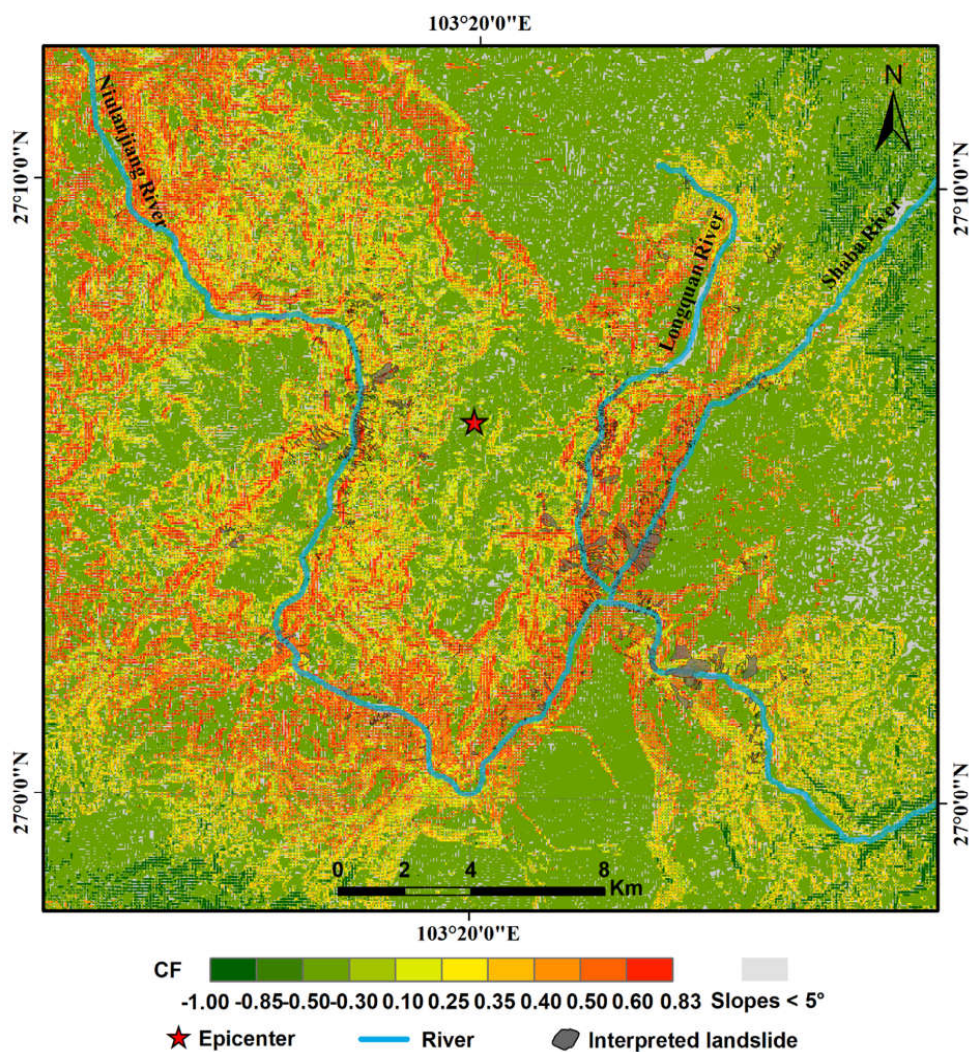




518

519 **Fig. 13.** Map showing predicted displacements in the study area.

520



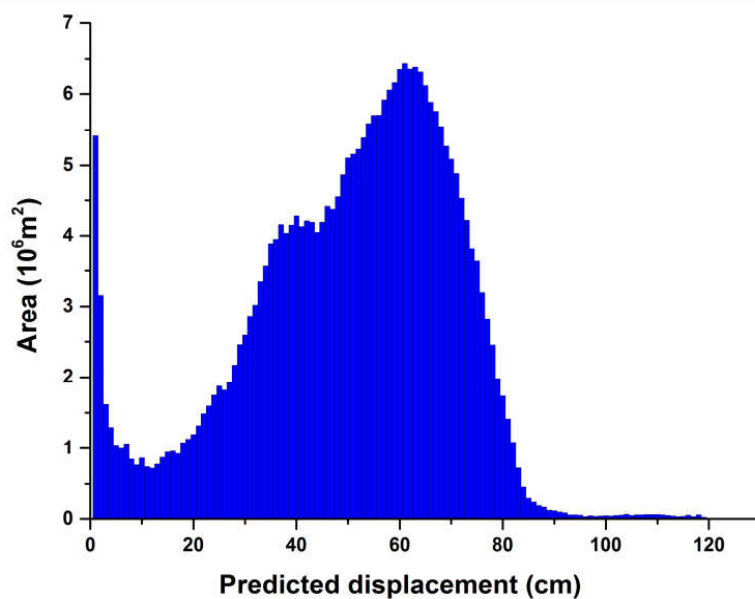
521

522 **Fig. 14.** Map showing probability of coseismic landslides in the Ludian earthquake. Probability

523 is portrayed in terms of values of *CF*.

524

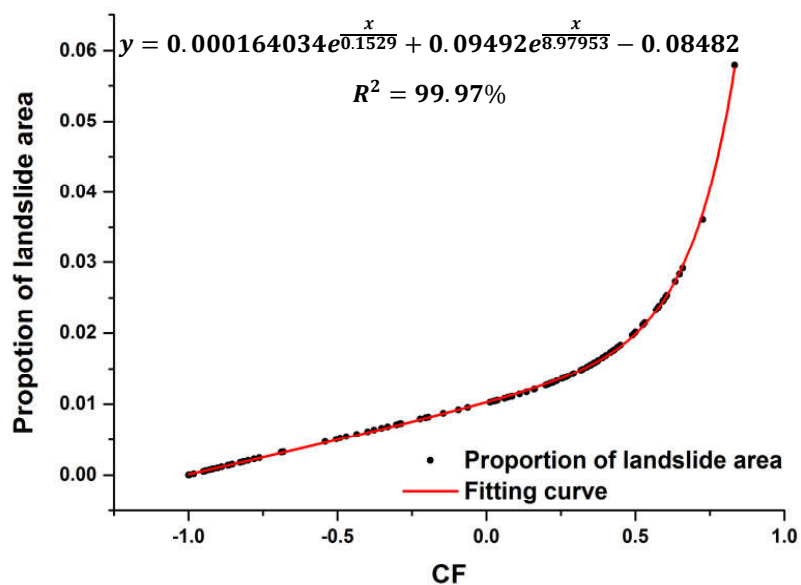
525



526

527 **Fig. 15.** Statistics data display the area of each predicted displacement.

528



529

530 **Fig. 16.** Proportion of the area of landslides lying in each *CF*-value area. A dot shows the
531 proportion of landslide area within an area of *CF* value; the red line is the fitting curve of the
532 data using second order exponential growth function.

533



534 **Table Captions**

535 **Table 1.** Shear strengths assigned to rock types in the study area

536

537



538 **Table 1**

539 Shear strengths assigned to rock types in the study area

| Rock type | γ (kN/m ³) | φ_b | JCS_0 (MPa) | JRC_0 | References |
|-----------|-------------------------------|-------------|------------------|---------|--------------------------|
| Slate | 26.5 | 28° | 130 | 3 | Coulson, 1972 |
| | | | | | Barton and Choubey, 1977 |
| | | | | | Bandis et al., 1983 |
| | | | | | Alejano et al., 2012 |
| Limestone | 21.5 | 34° | 100 | 9 | Yong et al., 2018 |
| | | | | | Bandis et al., 1983 |
| | | | | | Singh et al., 2012 |
| | | | | | Yong et al., 2018 |
| Basalt | 27.9 | 36° | 205 | 4 | Coulson, 1972 |
| | | | | | Barton and Choubey, 1977 |
| | | | | | Alejano et al., 2014 |
| Dolomite | 25.9 | 32° | 140 | 9.5 | Singh et al., 2012 |
| | | | | | Giusepone, 2014 |
| | | | | | Alejano et al., 2014 |

540